









>100-GHz Bandwidth Directly-Modulated Lasers and Adaptive Entropy Loading for Energy-Efficient >300-Gbps/ λ IM/DD Systems

Nikolaos-Panteleimon Diamantopoulos , *Member, IEEE, Member, OSA*, Hiroshi Yamazaki , *Member, IEEE*, Suguru Yamaoka, Munehiko Nagatani , *Member, IEEE*, Hidetaka Nishi, *Member, IEEE*, Hiromasa Tanobe, Ryo Nakao, Takuro Fujii , *Member, IEEE*, Koji Takeda , *Senior Member, IEEE*, Takaaki Kakitsuka , *Member, IEEE*, Hitoshi Wakita, Minoru Ida , Hideyuki Nosaka , *Senior Member, IEEE*, Fumio Koyama, *Fellow, IEEE, Fellow, OSA*, Yutaka Miyamoto, *Member, IEEE*, and Shinji Matsuo, *Fellow, IEEE*

(Post-Deadline Paper)

Abstract—We demonstrate DML-based net 325-Gb/s at back-to-back and 321.24-Gb/s after 2-km standard single-mode fiber transmissions for >300-Gbps/ λ short-reach optical interconnects. Our net rate performance denotes an increase of $\sim 34\%$ compared to our previous works, while the pre-FEC rates are >400 Gbps. The DML transmitter is based on a PPR-enhanced, >100-GHz-bandwidth DML, fabricated by our novel membrane-III-V-on-SiC technology. Also wide-band, entropy-loaded DMT modulation is utilized based on a novel adaptive algorithm and via a digitally-preprocessed analog multiplexer. These results pave the way towards low-cost and energy-efficient Terabit Ethernet and a significant step towards achieving DML-based 400-Gbps/ λ IM/DD systems in the future.

Manuscript received June 25, 2020; revised August 12, 2020; accepted August 24, 2020. Date of publication September 4, 2020; date of current version February 2, 2021. (Corresponding author: Nikolaos-Panteleimon Diamantopoulos.)

Nikolaos-Panteleimon Diamantopoulos, Suguru Yamaoka, Hidetaka Nishi, Ryo Nakao, Takuro Fujii, Koji Takeda, Hitoshi Wakita, Minoru Ida, and Shinji Matsuo are with NTT Device Technology Labs, Nippon Telegraph and Telephone Corporation, Atsugi, Kanagawa 243-0198, Japan (e-mail: np.diamantopoulos.pb@hco.ntt.co.jp; suguru.yamaoka.hm@hco.ntt.co.jp; hidetaka.nishi.sf@hco.ntt.co.jp; ryo.nakao.kb@hco.ntt.co.jp; takuro.fujii.uc@hco.ntt.co.jp; koji.takeda.vk@hco.ntt.co.jp; hitoshi.wakita.uc@hco.ntt.co.jp; minoru.ida.su@hco.ntt.co.jp; shinji.matsuo.vm@hco.ntt.co.jp).

Hiroshi Yamazaki, Munehiko Nagatani, and Hideyuki Nosaka are with NTT Device Technology Labs, Nippon Telegraph and Telephone Corporation, Atsugi, Kanagawa 243-0198, Japan, and also with NTT Network Innovation Labs, Nippon Telegraph and Telephone Corporation, Yokosuka, Kanagawa 239-0847, Japan (e-mail: hiroshi.yamazaki.mt@hco.ntt.co.jp; munehiko.nagatani.uh@hco.ntt.co.jp; hideyuki.nosaka.fb@hco.ntt.co.jp).

Hiromasa Tanobe is with NTT Device Innovation Center, Nippon Telegraph and Telephone Corporation, Atsugi, Kanagawa 243-0198, Japan (e-mail: hiromasa.tanobe.pt@hco.ntt.co.jp).

Takaaki Kakitsuka was with the NTT Device Technology Labs, Nippon Telegraph and Telephone Corporation, Atsugi, Kanagawa 243-0198, Japan, and now he is with the Graduate School of Information, Production and Systems, Waseda University, Kitakyushu, Fukuoka 808-0135, Japan (e-mail: t.kakitsuka@waseda.jp).

Fumio Koyama is with the Institute of Innovative Research, Tokyo Institute of Technology, Yokohama, Kanagawa 226-8503, Japan (e-mail: koyama.f.aa@m.titech.ac.jp).

Yutaka Miyamoto is with NTT Network Innovation Labs, Nippon Telegraph and Telephone Corporation, Yokosuka, Kanagawa 239-0847, Japan (e-mail: yutaka.miyamoto.fb@hco.ntt.co.jp).

Color versions of one or more of the figures in this article are available online at <https://ieeexplore.ieee.org>.

Digital Object Identifier 10.1109/JLT.2020.3021727

Index Terms—Adaptive entropy loading, direct-detection, directly-modulated laser.

I. INTRODUCTION

THE surging traffic growth in data center networks imposed by the increasing video and cloud content push future standardizations, such as the Terabit Ethernet (TbE) [1], to extend the line rate requirements beyond 200-Gbps per channel with the possibility of relying on 300- or 400-Gbps/channel in the near future. Even though current optical coherent systems can support such a trend in terms of throughput, intensity-modulated directly-detected (IM/DD) systems are more suitable to meet additional stringent requirements related to cost-per-bit, power consumption, and device footprints. In particular, IM/DD systems that utilize wide-bandwidth directly-modulated lasers (DMLs) [2]–[5] are arguably the most energy-efficient approach, which could pose such lasers among the leading technologies to support ICT growth in the future.

Recently we demonstrated the first-ever DMLs capable of achieving modulation bandwidths in excess of 100 GHz [5], which allowed us to reach 256-Gbps (net ~ 240 -Gbps) 4-level pulse amplitude modulation (PAM-4) transmissions [5]. This unprecedented performance was owed to our novel membrane-III-V-on-SiC technology [6] and a photon-photon resonance (PPR)-supporting compound-cavity design. In particular, our membrane-III-V-on-SiC technology benefits from both a high optical confinement factor and from the high thermal conductivity properties of the SiC substrate.

Meanwhile, techniques to expand the electrical signaling and the modulation bandwidth are in need in order to keep pace with fast-growing bandwidths of photonic transceivers [7]–[14]. Regarding the electrical bandwidth, our previously-demonstrated digitally pre-processed analog multiplexer (AMUX) [7]–[9] can effectively double the available electrical bandwidth and have achieved analog bandwidths in excess of 100-GHz [9]. On the other hand, the signaling can benefit better from multi-carrier/band modulations [10]–[14] compared to single-carrier

TABLE I
DATA RATES ACHIEVED IN THIS WORK

	NET RATE	PRE-FEC RATE
Back-to-Back	325 Gbps	411.66 Gbps
2-km SSMF	321.24 Gbps	407.95 Gbps

formats such as PAM-4, as the former match the available frequency-dependent signal-to-noise ratio (SNR) (caused, e.g., by PPR) better. In particular, the application of probabilistically-shaped (PS) constellations [15] in a sub-band/carrier basis – commonly referred to as “entropy loading” (EL) [10]–[12]–, provides additional flexibility in terms of networking and achievable rate.

By combining an adaptive algorithm for EL discrete multi-tone (EL-DMT) modulation with an AMUX for driving a >100-GHz bandwidth DML-on-SiC, we successfully demonstrated net 325-Gb/s and 321.24-Gbps at back-to-back (BTB) and after 2-km of standard single-mode fiber (SSMF) transmissions, respectively, surpassing our previous net rate by ~34% [16]. As listed in Table I, pre forward-error correction (FEC) rates actually exceeded 400 Gbps. In this extended paper, we expand on the obtained results of [16], while additionally providing a detailed description of a novel adaptive EL technique used.

The paper is organized as follows. Following the introduction in Section I, the adaptive entropy loading technique is discussed in detail in Section II. Section III focuses on the device aspects of this work (DML and AMUX) with particular emphasis on the DML design and characteristics. At last, the experimental demonstration is presented in Section IV, following a conclusion in Section V.

II. ADAPTIVE ENTROPY LOADING

In order to achieve single-channel IM/DD operations with >300 Gbps in an effective and power-efficient manner, optical transceivers with large analog bandwidths of >65 GHz are required [3], [10], [16]. When it comes to such wide-bandwidth optical transceivers, a flat end-to-end system frequency response is rarely achieved without the support of some advanced digital signal processing (DSP) technique. Furthermore and more importantly, even if a flat response is achieved through the use of, e.g., nonlinear equalization and/or pulse-shaping, the overall SNR will most probably still vary over different frequencies, posing limitations in single-carrier modulation formats such as PAM-4. An alternative solution which alleviates the limitations of single-carrier modulations, is the use of multi-carrier modulation formats such as, e.g., DMT in which quadrature-and-amplitude modulated (QAM) symbols with different modulation orders are assigned to different frequency subcarriers [13], [14]. In addition, non-quantized bit resolutions, i.e., in the form of probabilistically-shaped (PS) modulations, can address the SNR in a more efficient way and achieve capacities closer to the Shannon limit [15]. The modulation scheme in which a multi-carrier modulation relies on PS-QAMs is called “Entropy Loading” (EL) [10]–[12]. In such a scheme, different subcarriers or sub-bands are modulated by PS-QAMs with information entropies (expressed in [bits/symbol]) that are based on their SNR profile as shown in Fig. 1 for the DMT case.

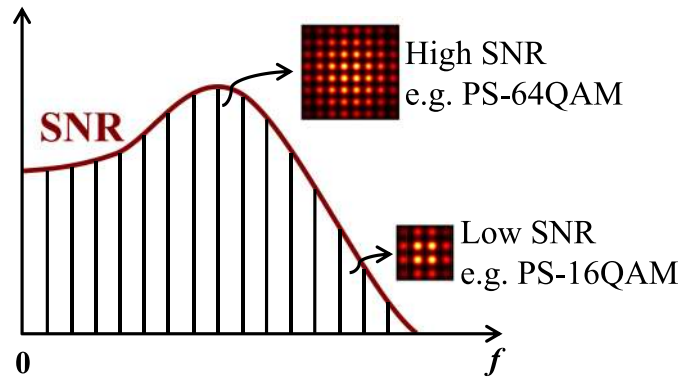


Fig. 1. EL-DMT: entropy loading in DMT modulation.

Considering such approaches, a question arises on how to assign PS-QAMs’ entropies in different sub-carriers/bands in the most efficient, simple, and accurate way in order to support the highest throughput or the lowest error performance possible. Previous works treated this entropy assignment problem on either a manual (e.g., human-in-the-loop) fashion [10] or by utilizing pre-calculated 3D look-up tables [12]. However, the former approach is difficult to be scaled up for a large number of sub-carriers/bands (typically hundreds for, e.g., DMT), while the latter can achieve only limited entropy resolutions (defined by the matrix size) while requiring extensive simulations in order to build the 3D matrices in the first place.

An alternative solution is the use of an adaptive/learning algorithm which attributes the entropy profiles based on a learning rule that ensures either maximization of the throughput or minimization of the error performance for a given data rate. This “machine-learning” approach can achieve arbitrary small information entropy resolutions and can be extended to a large number of subcarriers based on a single unified performance metric such as the “effective” normalized generalized mutual information (NGMI) [10], [17]. A possible drawback is that a number of communication loops are then required between the transmitter (Tx) and the receiver (Rx) for achieving adaptation convergence. However, the number of iterations can be minimized through an appropriate choice for the learning algorithm and initial conditions. In addition, after the initial adaptation is established, the system can then operate without any further communication between Tx and Rx, with no additional latency added. In this work, due to its rapid-convergence properties, we rely on a vectorial Newton’s method to solve the entropy assignment problem.

Following a DMT notation, the modulator assigns S subcarriers with PS-QAM modulations based on modulation orders M_i and entropies $H(X_i) = -\sum_{x \in X_i} P_i(x) \log_2 P_i(x)$. Here $i = 1, 2, \dots, S$ is the subcarrier index, X_i is the set of all possible symbols for the i -th subcarrier, and $P_i(\cdot)$ defines probability distributions. The entropies are given in [bits/symbol]. We consider PS-QAM based on Maxwell-Boltzmann (MB) statistics as follows:

$$P_i(x) \equiv P_{X_i}(x, v_i) = \frac{e^{-v_i|x|^2}}{\sum_{x' \in X_i} e^{-v_i|x'|^2}} \quad (1)$$

where v_i is the MB constant that defines the PS profile in each subcarrier. In such a system the net data rate after removing any FEC coding is given by [8], [10], [15]:

$$\begin{aligned} \text{NetRate}(\mathbf{v}) &= r_{\text{mod}} \sum_i R_{s,i} [H(X_i) \\ &\quad - (1 - r_{\text{FEC}}) \log_2(M_i)] \end{aligned} \quad (2)$$

where \mathbf{v} defines a vector with all v_i values, $R_{s,i}$ is the symbol rate per subcarrier, r_{mod} is a code rate defining any overhead required for synchronization, equalization, and modulation, and r_{FEC} is the FEC code rate. Note that, here, r_{FEC} is based on non-shaped parity bits while r_{mod} is applicable on shaped modulated symbols. As discussed, the most common performance metric in such multi-carrier PS modulations is the “effective” NGMI, which can be defined as follows [10], [17]:

$$\begin{aligned} \text{NGMI}(\mathbf{v}) &\approx 1 - \sum_i \left[H(X_i) \right. \\ &\quad \left. - \frac{1}{N} \sum_n \log_2 \frac{q_i(y_{n,i}|x_{n,i})}{\sum_{x' \in \mathcal{X}_i} q_i(y_{n,i}|x') P_i(x')} \right] / \sum_i m_i \end{aligned} \quad (3)$$

where $m_i = \log_2(M_i)$, $n = 1, 2, \dots, N$ is the sample instance (for N total samples), and $q_i(y_i|x_i)$ is the conditional probability which defines an auxiliary channel with input signal x_i and output signal y_i . Please note that, here, the expression for the achievable rate [15], [18] was used for mathematical convenience. However, the adaptive method presented in this section can be equally applied to any (N)GMI definition (e.g., based on bit-wise log-likelihood ratios) [17], [18].

Here the additive white Gaussian noise (AWGN) channel is considered as follows:

$$\begin{aligned} q_i(y_i|x_i) &\equiv P_{Y_i|X_i}(y_i|x_i, \sigma_i) \\ &= \exp\left(-\frac{|y_i - x_i|^2}{2\sigma_i^2}\right) / \sqrt{2\pi\sigma_i^2} \end{aligned} \quad (4)$$

with σ_i^2 being the noise variance per subcarrier.

For the adaptive EL algorithm we first need to define the derivatives of the MB distributions, entropies, net rates, and NGMIs in respect to v_i or \mathbf{v} as follows:

$$\partial_{v_i} P_i(x) = P_i(x) \left[\sum_{x' \in \mathcal{X}_i} P_i(x') |x'|^2 - |x|^2 \right] \quad (5)$$

$$\partial_{v_i} H(X_i) = - \sum_{x \in \mathcal{X}_i} \partial_{v_i} P_i(x) \left[\log_2 P_i(x) + \frac{1}{\ln(2)} \right] \quad (6)$$

$$\partial_{\mathbf{v}} \text{NetRate}(\mathbf{v}) = r_{\text{mod}} \sum_i R_{s,i} \partial_{v_i} H(X_i), \quad (7)$$

and

$$\begin{aligned} \partial_{\mathbf{v}} \text{NGMI}(\mathbf{v}) &\approx - \sum_i [\partial_{v_i} H(X_i) \\ &\quad - \frac{1}{N \ln(2)} \sum_{n=1}^N \frac{\sum_{x \in \mathcal{X}_i} q_i(y_{n,i}|x) \partial_{v_i} P_i(x)}{\sum_{x \in \mathcal{X}_i} q_i(y_{n,i}|x) P_i(x)}] / \sum_i m_i \end{aligned} \quad (8)$$

TABLE II
DMT AND FEC PARAMETERS USED IN SIMULATIONS AND EXPERIMENTS

DMT Sampling rate	160 GHz
Number of subcarriers	512
(I)FFT size	1024
Payload symbols	460
Modulation formats	PS-256QAM, PS-64QAM, PS-16QAM
Combined training symbols (TS) and cyclic prefix (CP) overhead, rate	~1.9 %, 0.9814
FEC overhead, code rate	~21 %, 0.826 [19]
NGMI target	0.857 [19]

Similar expressions for $\partial_{\mathbf{v}} \text{NGMI}(\mathbf{v})$ can be derived for other (N)GMI definitions [17], [18].

Finally, based on Eqs. (1)–(8) we can assign the entropies in an adaptive manner based on a vectorial Newton’s method:

- for maximizing the net rate based on an NGMI target (NGMI^*):

$$\begin{aligned} \mathbf{v}_{j+1} &= \mathbf{v}_j \\ &\quad + [\text{NGMI}^* - \text{NGMI}(\mathbf{v}_j)] / \partial_{\mathbf{v}} \text{NGMI}(\mathbf{v}) |_{\mathbf{v}=\mathbf{v}_j} \end{aligned} \quad (9)$$

- for maximizing NGMI (i.e., minimizing errors) based on a target net rate (NetRate^*):

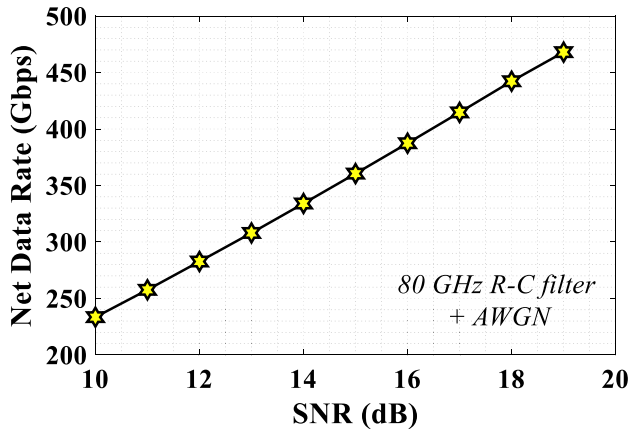
$$\begin{aligned} \mathbf{v}_{j+1} &= \mathbf{v}_j + [\text{NetRate}^* \\ &\quad - \text{NetRate}(\mathbf{v}_j)] / \partial_{\mathbf{v}} \text{NetRate}(\mathbf{v}) |_{\mathbf{v}=\mathbf{v}_j} \end{aligned} \quad (10)$$

Here j defines the iteration index. Based on the above rules, the iterative learning algorithm can then be performed based on the following algorithm: (i) define modulation orders M_i and initial MB coefficient vector \mathbf{v} , e.g., $\mathbf{v} = 0$, (ii) estimate the effective NGMI and NetRate after Tx-Rx communication, (iii) estimate MB coefficient vector \mathbf{v} based on Eq. (9) or Eq. (10), (iv) repeat (ii)-(iii) until performance target is reached. Step (i) can be based on rough empirical/experimental rules or easy-to-obtain (e.g., published) theoretical results, thus, avoiding any need for generating computationally costly 3D look-up tables.

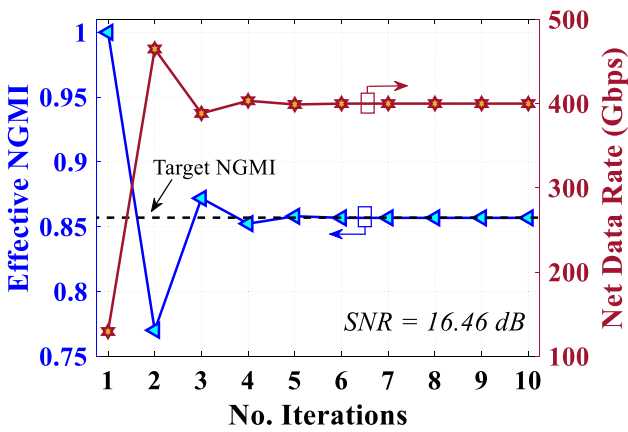
In the rest of the paper we focus on maximizing the net rate for a given effective NGMI target, i.e., using Eq. (9). The maximization of NGMI for a given net rate (i.e., Eq. (10)) is, therefore, left for future works.

Fig. 2(a) plots simulated results on the achieved net rate as a function of SNR based on EL-DMT with a sampling rate of 160 GHz and 512 subcarriers over a channel composed of an 80 GHz resistor-capacitor (R-C) filter and AWGN. These theoretical results match very closely the experimental results discussed in Section IV. The detailed DMT parameters are listed in Table II and were the same as those used in the experiments.

Finally, Fig. 2(b) depicts the convergence of the adaptive algorithm using Eq. (9) and SNR = 16.46 dB. In this case a steady-state net rate of 400.0 Gbps can be achieved using less than 6 iterations. Note that iteration #1 actually defines step (i) in the algorithm and, thus, the actual required number of iterations for the Newton’s algorithm to converge is less than 5. All points in Fig. 2(a) were calculated in a similar manner.



(a) SNR versus Net Data Rate.



(b) Iterations of the adaptive EL algorithm vs. Effective NGMI vs. Net Data Rate for SNR = 16.46 dB. Steady-state Net Data Rate = 400.0 Gbps. Steady-state Effective NGMI = Target NGMI = 0.857.

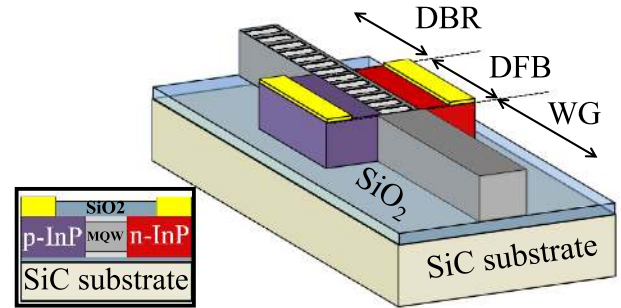
Fig. 2. Simulation results with an 80 GHz R-C filter + AWGN channel for EL-DMT with 160 GHz sampling rate and 512 subcarriers.

III. DEVICE CHARACTERISTICS

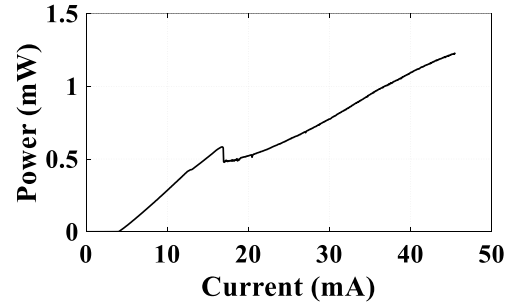
A. Membrane III-V-on-SiC Passive-Feedback Laser

The DML was fabricated using our membrane-III-V-on-SiC technology [6] and had a similar cavity design to the one in [5]. As a first step, a thin III-V membrane composed of InGaAlAs multi-quantum wells (MQWs) was directly-bonded to a SiC substrate through a SiO₂ buffer layer. The total III-V thickness was kept ~ 340 nm. Such a membrane-III-V-on-SiC structure enables a high optical confinement, while the high thermal conductivity of the SiC substrate ensures a high differential gain at high current densities. The combination of these two features allow for record-high relaxation oscillation frequencies of ~ 40 GHz and intrinsic 3-dB bandwidths of ~ 60 GHz [5].

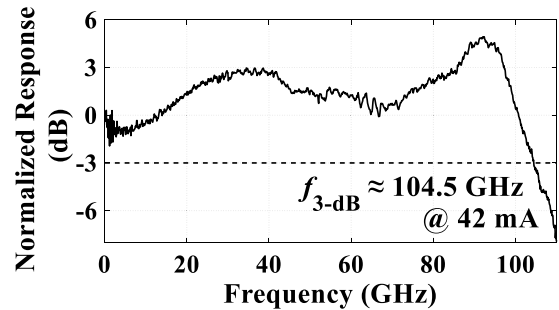
The cavity was based on the distributed reflector design shown in Fig. 3(a). In such a design, single-mode operation is provided by using a (passive) distributed Bragg reflector (DBR) section in order to filter one of the two main modes that appear in the transmittance spectrum of a non-phase-shifted (active) distributed feedback (DFB) section. Here, the DFB and DBR sections were 50- μm and 60- μm long, respectively, similar to



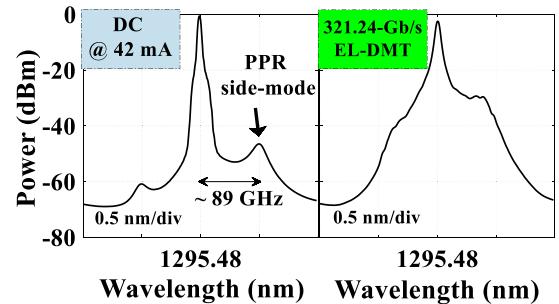
(a) Device schematic [5,6]. Inset: Cross-section.



(b) Fiber-coupled output power characteristics.



(c) EO response.



(d) Spectrum: w/o modulation (left), w/ EL-DMT modulation (right).

Fig. 3. Membrane DML-on-SiC.

[5]. In order to enhance the 3-dB bandwidth beyond the intrinsic value, a passive 135- μm long InP waveguide (WG) was also integrated in the side opposite to the DBR. That allowed for the generation of a PPR through a passive-feedback mechanism.

Fig. 3(b) and Fig. 3(c) depict the fiber-coupled output power and dynamic electro-optic (EO) response characteristics, respectively, at a stage-controlled room temperature of 25 $^{\circ}\text{C}$. The kink in Fig. 3(b) at ~ 17 mA is attributed to mode hopping. At

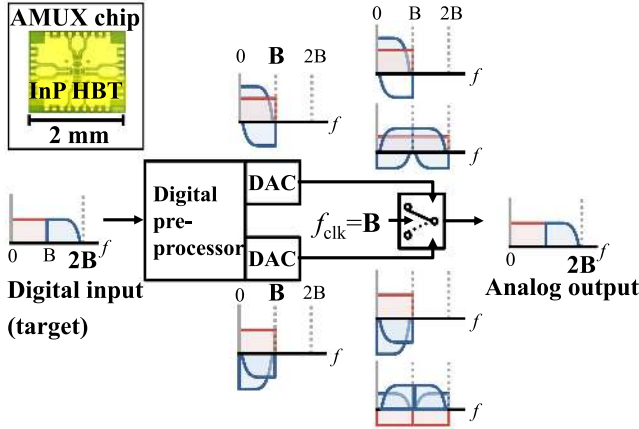


Fig. 4. Digitally pre-processed AMUX operation [7–9]. Inset: AMUX chip [9].

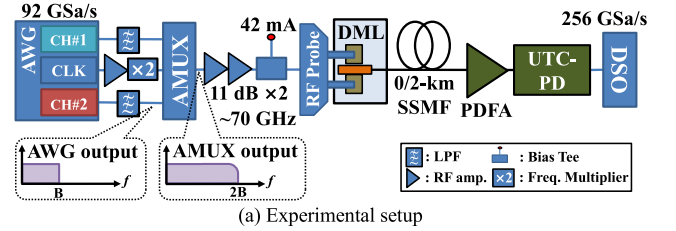
a bias current of 42 mA the laser exhibits a 3-dB bandwidth of ~ 104.5 GHz and a fiber-coupled power of ~ 0.6 dBm. Also, as shown in Fig. 3(d), at this bias current the lasing wavelength was ~ 1295.48 nm with a side-mode suppression ratio of >40 dB, and a PPR side-mode spaced at ~ 89 GHz. This side-mode spacing corresponds to the PPR peak appearing in the EO response. Finally, at these conditions the operating power was $42 \text{ mA} \times 4.233 \text{ V} \approx 0.178 \text{ W}$.

This time, the output power was <1 dBm which could be a limiting factor for practical short-reach applications. The relatively low output power was mainly because this fabrication run was among the first of this new technology and the slope efficiency was not yet optimized. In our more mature membrane InP on Si technology we can achieve slope efficiencies of $\sim 0.28 \text{ W/A}$ [20]. Hence, by optimizing our membrane InP on SiC technology to a similar degree, we expect that higher output powers of ~ 10 dBm can be reached in the near future. Moreover, the use of spot-size converters for efficient, low-loss fiber coupling is a complementary solution to the above [21].

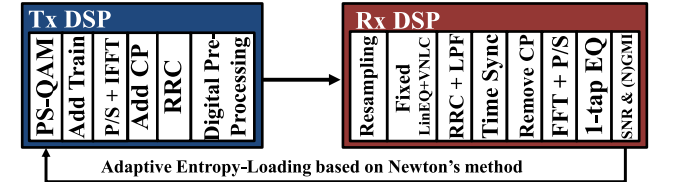
B. Digitally Pre-processed Analog Multiplexer

The detailed operation principle of the AMUX and its digital pre-processing are described in [7]–[9] and Fig. 4. With them, we can generate arbitrary signals with bandwidths up to $2B$ using two digital-to-analog converters (DACs) with an analog bandwidth of B . First, the DSP generates a digital signal corresponding to the wideband target signal. Then, the digital preprocessor weaves it into two sub-signals with a corresponding analog bandwidth of B . The digital sub-signals are converted to the analog sub-signals by the DACs. The AMUX makes these sub-signals pass through alternately at a clock frequency of $f_{clk} = B$ and outputs a superposition of the baseband components and images of the sub-signals. Based on the relative phases and amplitudes of the baseband signals and images, we can tailor the digital weaving process so that we obtain the target signal as the AMUX’s output.

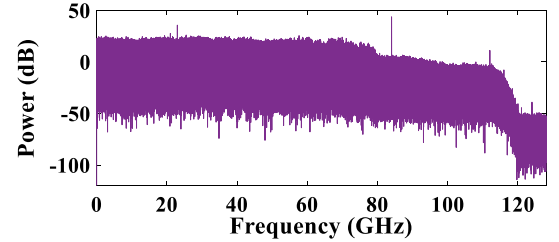
The AMUX was designed and fabricated by using a $0.25\text{-}\mu\text{m}$ -emitter-width InP Double Heterojunction Bipolar Transistor (DHBT) technology [9]. The cutoff and maximum



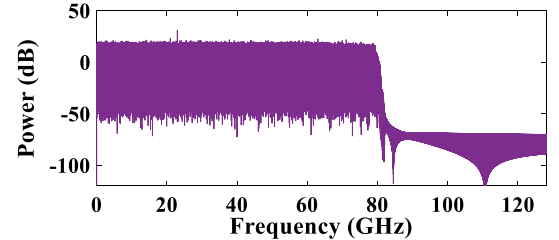
(a) Experimental setup



(b) DSP flowchart.



(c) Electrical spectrum after 2-km SSMF: after DSO.



(d) Electrical spectrum after 2-km SSMF: after VNLE+RRC+LPF.

Fig. 5. Experimental evaluation.

oscillation frequencies of the HBTs are up to 460 and 480 GHz, respectively, and their DC current gain is larger than 40. As shown in the inset of Fig. 4, the AMUX chip’s footprint is $2 \times 2 \text{ mm}^2$. The analog 3-dB bandwidth of the AMUX is larger than 100 GHz.

IV. EXPERIMENTAL DEMONSTRATION

A. Experimental Setup

The experimental setup is shown in Fig. 5(a). At the Tx side, two ~ 40 -GHz-bandwidth digitally-preprocessed baseband signals and a clock signal with a frequency of 41-GHz were generated by an arbitrary waveform generator (AWG) at ~ 92 GSa/s, in order to drive the AMUX. Prior to the AMUX, a set of ~ 40 -GHz-bandwidth low-pass filters (LPFs) were used to filter the baseband signals, while an electrical amplifier and a 2x frequency multiplier were used in order to amplify and double the frequency of the clock signal, respectively. To provide sufficient driving voltage (V_{pp}) for the DML, two ~ 70 -GHz-bandwidth, 11-dB-gain RF drivers were connected in series to

amplify the AMUX output. The laser was then driven using a ~ 70 -GHz-bandwidth bias-tee connected to an RF probe via a short RF cable. The laser was operating at a stage-controlled room temperature of 25 °C and its output was aligned to a lensed fiber pigtail which was connected to the SSMF. The driving current was 42 mA. A detailed discussion about DML's characteristics is given in Section III.A.

At the Rx side, in order to detect the ~ 80 -GHz bandwidth signal, an in-house uni-travelling-carrier photodiode (UTC-PD) was used together with a praseodymium-doped fiber amplifier (PDFA) to provide sufficient 9.1 dBm received optical power (ROP) as in [5]. The bandwidth of the in-house UTC-PD was > 90 GHz in the O-band, with a responsivity of ~ 0.1 A/W. Just before the PD, a 20 dB optical coupler (not shown in Fig. 5(a)) was used for ROP and spectrum measurements. Then, after the PD, the signals were stored by a > 100 -GHz real-time digital sampling oscilloscope (DSO) at 256-GSa/s. As discussed in Section III.A, we expect that in the near future we will be able to increase the DML's output power to up to ~ 10 dBm and, therefore, omit the use of a PDFA for practical applications. In addition, integration of the PD with a trans-impedance amplifier or use of PDs with better receiver sensitivity can reduce the required ROP effectively.

The offline DSP flowchart is shown in Fig. 5(b) and the DMT parameters are listed in Table II. Standard DMT processes were used including Hermitian-symmetric (inverse) fast Fourier transform ((I)FFT), serial-to-parallel (S/P) and parallel-to-serial (P/S) conversions, and addition of training symbols (TS) and cyclic prefix (CP) [14]. The DMT sampling rate was $R_s = 160$ GHz, the number of subcarriers was $S = 512$, and a total CP and TS overhead of $\sim 1.9\%$ was used (combined rate $r_{CP+TS} = 0.9814$). A 0.01-rolloff root-raised cosine (RRC) filter was used for pulse shaping at the Tx with a similar matched filter at the Rx. At the Rx DSP, the signals were first resampled at $2R_s$ and then equalized by a fixed (pre-trained) linear Wiener filter and an 11-tap 3rd-order Volterra nonlinear compensator (VNLC) followed by a low-pass filter (LPF) to remove residual clock components. The electrical spectrums after the DSO and after VNLC+RRC+LPF over 2-km SSMF transmissions as shown in Fig. 5(c) and Fig 5(d), respectively. Owing to the nonlinear equalization and filtering a flat spectrum could be obtained.

Regarding the EL profile, at first, fixed (non-PS) rectangular 256-QAM, 64-QAM, and 16-QAM were attributed to the subcarriers based on their QPSK-probed SNRs (Fig. 6) and simple empirical rules as step (i) of the algorithm described in Section II. Subcarriers with $\text{SNR} < 5$ dB were not used. Then, the entropies were optimized iteratively based on the vectorial Newton's method of Section II, Eq. (9) based on an "effective" NGMI target (see Section II for details).

B. Experimental Results

The effective NGMI versus the net and pre-FEC data rates for BTB and 2-km SSMF transmissions are summarized in Fig. 7 and Table I. In this work, the net rates were defined based on Eq. (2) by using $R_{s,i} = R_s/S$, $\forall i$ and $r_{mod} = r_{CP+TS}/2$. The division by 2 in the definition of r_{mod} encapsulates the use

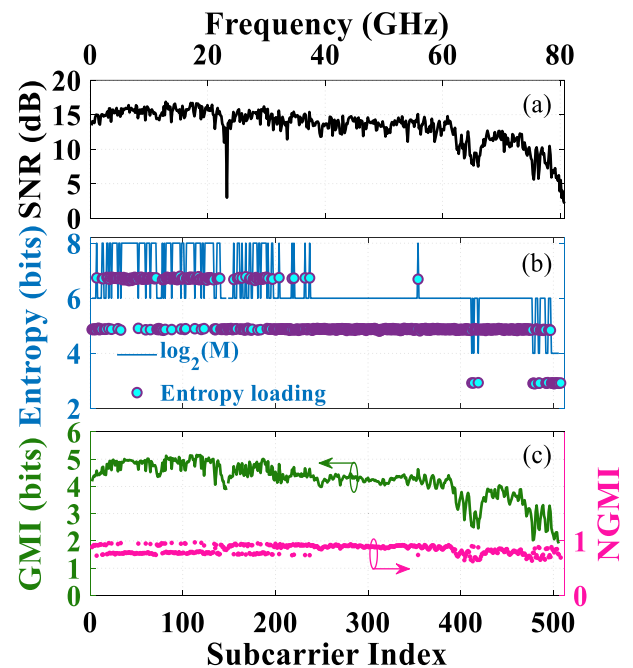


Fig. 6. Experimental results: (a) SNR, (b) Entropy Loading profile, and (c) (N)GMI per subcarrier after 2-km SSMF transmission at an NGMI target of 0.859. In this case, the net rate was 321.24 Gbps and a total of 505 subcarriers were used.

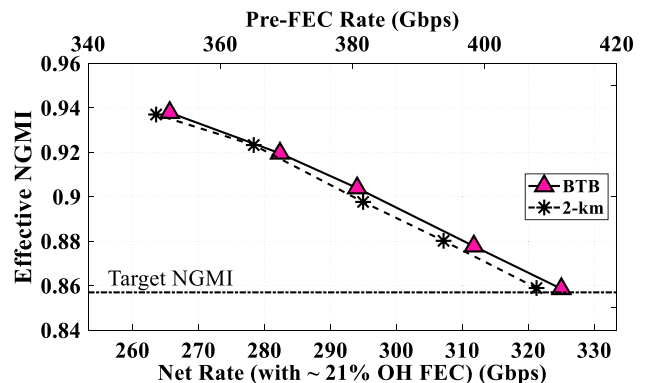


Fig. 7. Effective NGMI versus Net and Pre-FEC Data Rate.

of a 2x size (I)FFT, used for the Hermitian symmetry. Hence, it is considered here as part of the modulation. The system was re-trained for each data point by estimating the SNR and then adapting the EL-DMT for different target NGMIs using Eq. (9). The maximum NGMI target and FEC were based on a concatenated FEC with an aggregate overhead (OH) of $\sim 21\%$ (total code rate, $r_{FEC} = 0.826$) and an NGMI threshold of 0.857 [19]. Based on this 0.857 NGMI threshold, net 325-Gbps and 321.24-Gbps were achieved after BTB and 2-km SSMF transmissions, respectively. Regarding the 2-km SSMF transmission, these results denote an increase of $\sim 34\%$ compared to our previous work [5]. In addition, the pre-FEC rates (after removing the CP+TS) were 411.66 Gbps and 407.95 Gbps, respectively.

The SNR, entropy assignment, and (N)GMI profiles per subcarrier of the 321.24-Gb/s EL-DMT signal after 2-km SSMF

transmissions are shown in Fig. 6(a), Fig. 6(b), and Fig. 6(c), respectively. Also the modulated optical spectrum after the DML is shown in Fig. 3(d). In this case, the average SNR was ~ 13.3 dB. Based on this value, the obtained net rates are very close to the theoretical results shown in Fig. 2(a). Also, The SNR dip around 23-GHz (148-th subcarrier) corresponds to spurs appearing in the electrical spectrum of Fig. 5(d). Based on previous measurements that used the same AWG but had a different experimental setup, we believe that these spurs are actually caused by residual clock components of the AWG, i.e., $92/4 = 23$ GHz. Even though these SNR results can appear to be relatively low, there is a lot of room for improvement considering that the laser's power can be considerably increased in the future (see Section III.A). Meanwhile the main bandwidth limitation in our setup was coming from the RF drivers and the AWG. Future works, therefore, will be focused on optimizing our III-V/SiC technology to increase the laser's fiber-coupled fiber and also co-integrate the laser with the high-speed electronics. Then, based on the theoretical results of Fig. 2(a), net data rates of >400 Gbps can be expected in the future.

V. CONCLUSION

Towards low-cost and energy-efficient TbE and single-channel >300-Gbps IM/DD systems, we have demonstrated DML-based net 325-Gb/s at BTB and 321.24-Gb/s after 2-km SSMF transmission and pre-FEC rates >400 Gbps. The DML transmitter was based on a PPR-enhanced, >100-GHz-bandwidth DML fabricated by our novel membrane-III-V-on-SiC technology. Also wide-band, entropy-loaded DMT modulation was utilized based on a novel adaptive algorithm and via a digitally-preprocessed analog multiplexer. Our net rate performance denotes an increase of $\sim 34\%$ compared to our previous works, and it is a significant step towards achieving DML-based 400-Gbps/ λ IM/DD inter-connections in the future.

ACKNOWLEDGMENT

N.P.D. would like to thank Dr. T. Eriksson for the valuable discussions regarding probabilistic shaping and FEC.

REFERENCES

- [1] "2020 Ethernet Roadmap," Ethernet Alliance, 2020, [Online], Available: <https://ethernetalliance.org/technology/2020-roadmap/>.
- [2] S. Matsuo and T. Kakitsuka, "Low-operating-energy directly modulated lasers for short-distance optical interconnects," *Adv. Opt. Photon.*, vol. 10, no. 3, pp. 567–643, Sep. 2018.
- [3] Y. Matsui, R. Schatz, D. Che, F. Khan, M. Kwakernaak, and T. Sudo, "Isolator-free >67-GHz bandwidth DFB+R laser with suppressed chirp," in *Proc. OFC*, San Diego, CA, USA, 2020, Paper Th4A.1.
- [4] Y. M. Di Che, X. Chen, R. Schatz, and P. Iannone, "400-Gb/s direct modulation using a DFB+R laser," *Opt. Lett.*, vol. 45, no. 12, pp. 3337–3339, Jun. 2020.
- [5] S. Yamaoka *et al.*, "239.3-Gbit/s net rate PAM-4 transmission using directly modulated membrane lasers on high-thermal-conductivity SiC," in *Proc. ECOC*, Dublin, Ireland, 2019, Paper PD.2.1.
- [6] S. Yamaoka *et al.*, "High-temperature continuous-wave operation of 1.3- μ m membrane distributed reflector lasers on SiC," in *Proc. CLEO*, San Jose, CA, USA, 2019, Paper STu3N.6.
- [7] H. Yamazaki *et al.*, "IMDD Transmission at net data rate of 333 Gb/s using over-100-GHz-bandwidth analog multiplexer and Mach-Zehnder modulator," *J. Lightw. Technol.*, vol. 37, no. 8, pp. 1772–1778, Apr. 2019.

- [8] H. Yamazaki *et al.*, "Net-400-Gbps PS-PAM transmission using integrated AMUX-MZM," *Opt. Express*, vol. 18, no. 27, pp. 25544–25550, Sep. 2019.
- [9] M. Nagatani *et al.*, "An over-110-GHz-bandwidth 2:1 analog multiplexer in 0.25- μ m InP DHB technology," in *Proc. IMS*, Philadelphia, PA, USA, 2018, Paper We2A-1.
- [10] Xi Chen, J. Chandrasekhar, Cho, and P. Winzer, "Single-wavelength and single-photodiode entropy-loaded 554-Gb/s transmission over 22-km SMF," in *Proc. OFC*, San Diego, CA, USA, 2019, Paper Th4B.5.
- [11] D. Che and W. Shieh, "Approaching the capacity of colored-SNR optical channels by multicarrier entropy loading," *J. Lightw. Technol.*, vol. 36, no. 1, pp. 68–78, Jan. 2018.
- [12] D. Che and W. Shieh, "Squeezing out the last few bits from band-limited channels with entropy loading," *Opt. Express*, vol. 27, no. 7, pp. 9321–9329 Apr. 2019.
- [13] C. Kottke, C. Caspar, V. Jungnickel, R. Freund, M. Agustin, and N. N. Ledentsov, "High speed 160 Gb/s DMT VCSEL transmission using pre-equalization," in *Proc. OFC 2017*, Los Angeles, CA, USA, 2017, Paper W4I.7.
- [14] N. P. Diamantopoulos, T. Fujii, H. Nishi, K. Takeda, T. Kakitsuka, and S. Matsuo, "Energy-efficient 120-Gbps DMT transmission using a 1.3- μ m membrane laser on Si," in *Proc. OFC*, San Diego, CA, USA, 2018, Paper M2D.5.
- [15] F. Buchali, F. Steiner, G. Böcherer, L. Schmalen, P. Schulte, and W. Idler, "Rate adaptation and reach increase by probabilistically shaped 64-QAM: An experimental demonstration," *J. Lightw. Technol.*, vol. 34, no. 7, pp. 1599–1609, Apr. 2016.
- [16] N. P. Diamantopoulos *et al.*, "Net 321.24-Gb/s IMDD transmission based on a >100-GHz bandwidth directly-modulated laser," in *Proc. OFC*, San Diego, CA, USA, 2020, Paper Th4C.1.
- [17] J. Cho, L. Schmalen, and P. J. Winzer, "Normalized generalized mutual information as a forward error correction threshold for probabilistically shaped QAM," in *Proc. ECOC*, Gothenburg, Sweden, 2017, Paper M.2.D.2.
- [18] A. Alvarado, E. Agrell, D. Lavery, R. Maher, and P. Bayvel, "Replacing the soft-decision FEC limit paradigm in the design of optical communication systems," *J. Lightw. Technol.*, vol. 34, no. 2, pp. 707–721, Feb. 2016.
- [19] T. Kobayashi *et al.*, "35-Tb/s C-band transmission over 800 km employing 1-Tb/s PS-64QAM signals enhanced by complex 8×2 MIMO equalizer," in *Proc. OFC*, San Diego, CA, USA, 2019, Paper Th4B.2.
- [20] T. Fujii *et al.*, "1.3- μ m directly modulated membrane laser array employing epitaxial growth of InGaAlAs MQW on InP/SiO₂/Si substrate," in *Proc. ECOC*, Düsseldorf, Germany, 2016, Paper Th.3.A.2.
- [21] H. Nishi *et al.*, "Membrane distributed-reflector laser integrated with SiO_x-based spot-size converter on Si substrate," *Opt. Express*, vol. 24, no. 16, pp. 18346–18352, Aug. 2016.

Nikolaos-Panteleimon (Pandelis) Diamantopoulos (Member, IEEE) was born in Athens, Greece, in 1988. He received the B.Sc. degree from the University of Peloponnese, Peloponnese, Greece, in 2009, two M.Sc. degrees from Aston University, Birmingham, U.K., and Scuola Superiore Sant'Anna, Pisa, Italy, in 2012 under the joint-masters Erasmus Mundus program, and the Ph.D. degree from Osaka University, Osaka, Japan, in 2016. Between 2011 and 2016, he was involved in several EU-funded R&D projects at the Athens Information Technology (AIT) Research Center, Greece. Since 2016, he has been with NTT Device Technology Labs, Japan. His research interests include optical communications, digital signal processing, nonlinear dynamical systems, space-division multiplexing, and semiconductor lasers. He is a member of OSA.

Hiroshi Yamazaki (Member, IEEE) received the B.S. degree in integrated human studies and the M.S. degree in human and environmental studies both from Kyoto University, Kyoto, Japan, in 2003 and 2005, respectively, and the Dr. Eng. degree in electronics and applied physics from the Tokyo Institute of Technology, Tokyo, Japan, in 2015. In 2005, he joined NTT Photonics Laboratories, Kanagawa, Japan, where he has been involved in research on optical waveguide devices for communications systems. He is concurrently with NTT Network Innovation Laboratories and NTT Device Technology Laboratories, Atsugi, Japan, where he is involved in research on devices and systems for optical transmission using advanced multilevel modulation formats. He is a member of the IEICE.

Suguru Yamaoka was born in Osaka, Japan, in 1993. He received the B.E. and M.E. degrees in applied physics in 2015 and 2017, respectively, from Osaka City University, Osaka, Japan, where he is currently working toward the Ph.D. degree in applied physics. In 2017, he joined NTT Device Technology Laboratories, Atsugi, Japan. His research focuses on high-speed III–V semiconductor lasers on silicon carbide. He is a member of IEICE and JSAP.

Munehiko Nagatani (Member, IEEE), biography not available at the time of publication.

Hidetaka Nishi received the B.S. and M.S. degrees in mechanical science and engineering and the Ph.D. degree in electronics and applied physics from the Tokyo Institute of Technology, Tokyo, Japan, in 2005, 2007, and 2016, respectively. In 2007, he joined NTT Microsystem Integration Laboratories. Since then, he has been conducting research on integrated photonic and plasmonic devices. He is a member of OSA and JSAP.

Hiromasa Tanobe, biography not available at the time of publication.

Ryo Nakao, biography not available at the time of publication.

Takuro Fujii (Member, IEEE) was born in Kyoto, Japan, in 1986. He received the B.E. and M.E. degrees in system design engineering from Keio University, Yokohama, Japan, in 2010 and 2012, respectively. In 2012, he joined NTT Photonics Laboratories, Atsugi, Japan. His research interests include MOVPE growth of III–V semiconductors and the development of III–V semiconductor lasers on Si for photonic integrated circuits. He is a member of IEICE and JSAP. He was the recipient of the Young Scientist Presentation Award from the JSAP in 2014.

Koji Takeda (Senior Member, IEEE) received the B.S., M.S., and Ph.D. degrees in electronics engineering from the University of Tokyo, Tokyo, Japan, in 2005, 2007, and 2010, respectively. From 2008 to 2010, he received a Research Fellowship for Young Scientists from the Japan Society for the Promotion of Science. In 2010, he joined NTT Photonics Laboratories. His current research interests include ultralow-power optical interconnects, InP photonic integrated circuits, and photonic crystal lasers. He is a member of the IEICE and JSAP. He was the recipient of the Best Student Paper Award from the IEEE Photonics Society in 2009 and the Outstanding Student Presentation Award from the JSAP in 2010.

Takaaki Kakitsuka (Member, IEEE) was born in Kumamoto, Japan, in 1971. He received the B.S. and M.S. degrees in physics and the Dr. Eng. degree from Kyushu University, Fukuoka, Japan, in 1994, 1996, and 2012, respectively. In 1996, he joined NTT Opto-Electronics Laboratories, NTT Corporation, Atsugi, Japan. From 1996 to 2019, he was involved in research on semiconductor lasers and optical integrated devices at NTT Corporation. In 2019, he became an Associate Professor with the Graduate School of Information, Production and Systems, Waseda University, Fukuoka, Japan. His research focuses on semiconductor lasers and their information communication system applications. He is a member of IEICE, JSAP, and the Physical Society of Japan.

Hitoshi Wakita, biography not available at the time of publication.

Minoru Ida, biography not available at the time of publication.

Hideyuki Nosaka (Senior Member, IEEE) received the B.S. and M.S. in physics from Keio University, Yokohama, Japan, in 1993 and 1995, respectively, and the Dr.Eng. in electronics and electrical engineering from the Tokyo Institute of Technology, Tokyo, Japan, in 2003. He joined NTT Wireless System Laboratories in 1995, where he was engaged in R&D of monolithic microwave ICs and frequency synthesizers. Since 1999, he has been involved in R&D of ultrahigh-speed mixed-signal ICs for optical communications systems at NTT Photonics Laboratories. He is currently a Senior Research Engineer, Supervisor, and the Group Leader of the High-Speed Analog Circuit Research Group at NTT Device Technology Laboratories. He was the recipient of the 2001 Young Engineer Award and the 2012 Best Paper Award by IEICE. He is a member of IEICE and IEEE.

Fumio Koyama, biography not available at the time of publication.

Yutaka Miyamoto (Member, IEEE), biography not available at the time of publication.

Shinji Matsuo (Fellow, IEEE) received the B.E. and M.E. degrees in electrical engineering from Hiroshima University, Hiroshima, Japan, in 1986 and 1988, respectively, and the Ph.D. degree in electronics and applied physics from the Tokyo Institute of Technology, Tokyo, Japan, in 2008. In 1988, he joined NTT Optoelectronics Laboratories, where he researched photonic functional devices using multiple quantum well pin modulators and VCSELs. In 1997, he researched optical networks using WDM technologies at NTT Network Innovation Laboratories. Since 2000, he has been researching high-speed tunable optical filters and lasers at NTT Photonics Laboratories, Atsugi, Japan, and NTT Device Technology Laboratories, Atsugi, Japan. He is a Senior Distinguished Researcher of NTT. He is a member of JSAP and IEICE.